Journal of Electronic Materials (2024) 53:5961–5970
https://doi.org/10.1007/s11664-024-11158-x

28TH INTERNATIONAL CONFERENCE ON NUCLEAR TRACKS AND RADIATION MEASUREMENTS

Increased Green Electricity Generated in Carbon-Doped TiO_2-Based Hydroelectric Cell

Kajal[1] · Sunidhi Badola[2] · Abha Shukla[2] · Jyoti Shah[2] · Deepika[1] · Rajesh Kumar[1]

Received: 12 March 2024 / Accepted: 29 April 2024 / Published online: 2 June 2024

Abstract
The most efficient way to mitigate the degradation of the environment and global warming is to generate clean, sustainable green energy. A hydroelectric cell (HEC) is a green energy device that employs oxygen-deficient, mesoporous metal oxides to produce electricity through water splitting at room temperature. In this work, carbon doping is explored to create oxygen vacancies in TiO_2. The solid-state reaction method was used to process titanium dioxide (TiO_2) with 0.1 wt.% and 0.5 wt.% of carbon (C). Photoluminescence (PL) spectroscopy confirmed the presence of microstructural defects and optical defects in the carbon-doped TiO_2. The enhancement in microstrain and dislocation density due to the incorporation of carbon atoms in the TiO_2 lattice was confirmed by x-ray diffraction (XRD) analysis. The HEC was fabricated by applying silver paste in a comb-like pattern to one face of the sample pellet and attaching a zinc sheet to the other face. The surface of the C-TiO_2 pellet was moistened with water to generate voltage and current. The fabricated 2×2 cm^2 TiO_2 and 0.1 wt.% and 0.5 wt.% C-doped TiO_2 HECs generated short-circuit current of 5.0 mA, 6.3 mA, and 7 mA with open-circuit voltage of 0.76 V, 0.81 V, and 0.74 V, respectively. The cells delivered off-load output power of 3.8 mW, 5.10 mW, and 5.2 mW, respectively. Nyquist curves obtained for the HECs in the wet state confirmed the ionic conduction process within the material and charge transfer to the electrodes. Carbon-doped TiO_2 processed at low temperature generated enhanced power output in comparison to pure TiO_2. Therefore, C-doped TiO_2 is a cost-effective material for producing green electricity at a large scale.

Keywords Hydroelectric cell · green electricity · titanium dioxide · XRD · V–I measurements · Raman · SEM

Introduction

The excessive consumption of non renewable resources and effects of climate change are two major concerns society is facing nowadays. The long-standing energy-related problems of developing countries might be overcome by renewable energy sources and technologies. The need for novel resources and techniques for generating energy is prompted by a growing need for sustainable and clean energy sources.

Current energy sources comprise solar cells, lithium batteries, and other electrochemical batteries, all of which present operational hazards, waste challenges, and environmental drawbacks.[1,2] Humanity would benefit greatly from long-term, economically viable, and sustainable energy production strategies centered on abundant, renewable resources such as water, wind, and solar energy.[3] There have been multiple attempts to utilize water or water vapor as a source of electrical energy, but little progress has been achieved in this field. The hydroelectric cell (HEC), which is a recently introduced renewable source of energy, generates green electricity by the dissociation of water molecules at room temperature through engineered oxygen-deficient and porous materials without the use of any acid, alkali, light, or electrolyte,[4–9] in line with current energy source requirements. The HEC simply generates electricity using water alone, eliminating the consumption of hazardous chemicals. For the fabrication of the HEC, the material synthesized should be highly nonporous and enriched with

✉ Rajesh Kumar
rajeshkumaripu@gmail.com

[1] University School of Basic and Applied Sciences, Guru Gobind Singh Indraprastha University, New Delhi 110078, India

[2] CSIR, National Physical Laboratory, New Delhi 110012, India

defect centers, especially oxygen vacancies. Oxygen vacancies, which serve as the F-centers and dangling bonds, are essential in describing the absorption and chemidissociation of water molecules on metal oxides.[10] Hydrogen production, photocatalysis, humidity sensing, gas sensing, and various other processes also utilize the concept of molecule dissociation at surfaces.[11–15] Oxygen vacancies produce surface dangling bonds, resulting in a powerful electric field for water dissociation.[16] HECs are fabricated by coating silver paste in a comb-shaped pattern onto one face of the sample pellet and attaching a zinc sheet to the other side. Once the water comes into contact with the material, it forms a chemisorbed layer on the surface. Multiple water layers are physisorbed onto the chemisorbed layer, facilitating proton hopping within these layers via the Grotthuss mechanism. These hopping protons when trapped inside the nano-pores create a high electric field, able to dissociate water in physisorbed layers. The physidissociated ions move toward the respective electrode. An electromotive force (EMF) and current are subsequently generated due to the electrochemical reaction at the electrodes. An oxidation reaction occurs at the zinc electrode which reacts with hydroxide ions and forms zinc hydroxide, whereas a proton reduction reaction occurs at the silver cathode forming hydrogen gas. Because of the outstanding chemical stability and efficiency of production, porous oxide materials have gained increasing prominence as functional materials in recent years.[17–19] Water molecules can easily travel through the pores of a porous oxide ceramic material, and vacancies contribute to a large effective surface area.[20] Numerous metal oxides have been explored for use in HECs, including SnO_2, MgO, ZnO, TiO_2, WO_3, CeO_2, and $SrTiO_3$.[21–27]

The family of transition metal oxides includes TiO_2, which is an inert material with high photocatalytic activity due to strong oxidizing properties (with a wide surface area), chemical stability, and biocompatibility. It features a low production cost and high dielectric constant, and is a cheap material. TiO_2 is a large-bandgap semiconductor with bandgaps of 3.2 and 3.0 eV for the anatase and rutile phases.[28,29] Oxygen vacancies form by heating pure TiO_2 at high temperatures in an inert atmosphere.[30] Shukla et al.[31] reported that pure TiO_2-based HECs generated power of 2.07 mW, whereas HECs of Mg-doped TiO_2, Li-doped TiO_2, and Fe-doped TiO_2 produced 5.55 mW, 2.88 mW, and 0.36 mW. Bhakar et al.[9] reported a HEC of $BaTiO_3$ which generated an output electrical power of 3.57 mW. The current research is focused on enhancing the output electrical power of TiO_2 -based cells. The power output of carbon-doped TiO_2-based HECs is explored in this study due to its low-cost availability and ability to achieve significant electrical conduction. The solid-state reaction method was used to synthesize carbon-doped TiO_2 nanoparticles. Doping carbon in TiO_2 is known to introduce oxygen vacancies, various surface defects, grain boundaries, and interfaces that result in an increase in conductivity. To improve the electrical power, carbon-doped TiO_2-based HECs of various compositions were fabricated and tested.

Experimental Section

Preparation of C-Doped TiO_2

High-purity titanium dioxide (TiO_2) powder (Sigma Aldrich) and graphite (C) powder (Sigma Aldrich) precursors were used in the synthesis of carbon-doped TiO_2 nanoparticles.

Samples of 0.1 wt.% and 0.5 wt.% carbon-doped TiO_2 were synthesized using the solid-state reaction method. For better homogenization, wet grinding was carried out in acetone with a pestle and mortar for 30 min. The ground powders were calcined for 5 h at 400°C in a muffle furnace. The pre-sintered powder was pelletized into 2×2 cm^2 pellets and sintered at 600°C. Pure TiO_2 was designated as sample A, whereas TiO_2 samples with 0.1 wt.% and 0.5 wt.% carbon were designated as samples B and C, respectively.

To fabricate the HECs from the sintered pellets, conducting silver paste was applied in a comb pattern to one face of each pellet to serve as the cathode, and a zinc sheet was attached to the other face of the pellet as the anode. Ohmic electrical contacts were made on electrodes to measure the power output from the cell.

Characterization of C-Doped TiO_2 HEC

Characterization of the synthesized samples was performed using various instrumental techniques. For phase identification, an x-ray diffraction (XRD) pattern was obtained with a Bruker AXS D8 Advance diffractometer using Cu-Kα radiation with a wavelength of 0.154 nm. Detailed information about the chemical structure, phase composition, and defect characteristics of samples A, B, and C prepared by heat treatment was obtained by Raman spectroscopy (IndiRAM CTR-300 spectrometer) using a semiconductor laser of 532 nm and power of 15 mW at room temperature. Field-emission scanning electron microscopy (FESEM) was performed using an FEI Nova NanoSEM 450 at an accelerating voltage of 15 kV to acquire detailed information about the surface morphology related to the shape, structure, and particle size of C-doped TiO_2. A PerkinElmer LS 55 fluorescence spectrometer was used to examine the defects such as oxygen vacancies produced by carbon doping in TiO_2 at an excitation wavelength of 320 nm. Voltage–current (V–I) characteristics were plotted using a Keithley 2430 1 kW source meter. The Nyquist curves for the HECs fabricated from samples A, B, and C

were obtained on a Wayne Kerr 6500B impedance analyzer in the frequency range of 20 Hz to 120 MHz.

X-ray Diffraction (XRD)

For phase identification and determination of microstrain development in TiO_2 by carbon doping, x-ray diffraction was performed. The crystallite size was calculated for all the synthesized samples A, B, and C using the Debye–Scherrer equation[32]:

$$D = k\lambda/\beta cos\,\theta \quad (1)$$

where D is the crystallite size, K is the Scherrer constant with a value of 0.9, λ is the wavelength of the Cu-Kα radiation (0.154 nm), β is the full width at half-maximum, and θ is the Bragg angle. The x-ray diffraction patterns of samples A, B, and C are shown in Fig. 1. The peaks observed at 25.37°, 37.86°, 48.08°, 53.89°, 55.08°, 62.74°, 68.83°, 70.36°, and 75.10° in the XRD pattern correspond to the (101), (004), (200), (105), (211), (204), (116), (220), and (215) crystal planes of anatase TiO_2, which matches well with JCPDS 21-1272. The (110), (200), and (202) crystal planes at 37.01°, 38.6°, and 76.01° correspond to rutile TiO_2, which matches well with JCPDS 21-1276. The phase of pure TiO_2 was not affected by the addition of carbon atoms. The high content of carbon (0.5wt.%) decreased the intensity of the XRD as compared to pure TiO_2 and TiO_2 with low (0.1 wt.%) carbon doping, due to lattice distortion. This resulted in the broadening of peaks and a decrease in the crystallinity of sample C.[33]

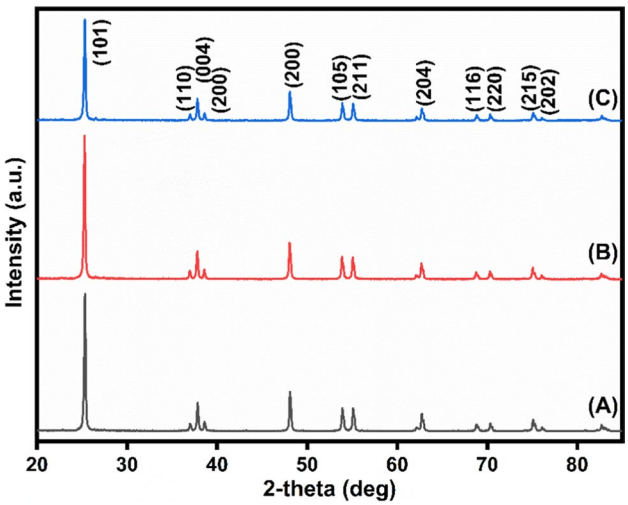

Fig. 1 XRD spectra of (A) pure TiO_2, (B) 0.1 wt.% carbon-doped TiO_2, and (C) 0.5 wt.% carbon-doped TiO_2.

The average crystallite size for samples A, B, and C was calculated as 45.21 nm, 42.84 nm, and 40.69 nm, respectively. The doping of carbon inhibited the growth of nanoparticles. Hence, the crystallite size of the samples decreased with increased carbon doping.[34] According to an earlier report, carbon atoms can replace titanium and oxygen in the lattice sites, causing the dissociation of Ti–O bonds to form Ti–C and C–O bonds.[35] This results in lattice distortion and the creation of defects such as vacancies that induce strain in the crystal lattice and also act as nucleation sites for dislocations, hence leading to the formation of dislocation networks in the samples. The increased concentration of carbon in TiO_2 causes more distortion in the lattice which further enhances the microstrain, as shown in Table I.

The microstrain in the lattice was calculated using the Stokes–Wilson equation[36]:

$$\varepsilon = \beta/4\tan\theta \quad (2)$$

where ε is the microstrain, β is the full width at half-maximum (FWHM) of the most intense (101) plane, and θ is the Bragg angle.

The Williamson–Smallman equation[37] was used to calculate the dislocation density:

$$\delta = 1/D^2 \quad (3)$$

where D is the crystallite size and δ is the dislocation density.

The crystallite size, microstrain, and dislocation density calculated for the (101) plane from the XRD peak are given in Table I.

Raman Spectroscopy

Detailed information about the chemical structure, phase composition, defect characteristics, and crystallinity of

Table I The crystallite size, microstrain in the lattice, and dislocation density of samples A, B, and C

Sample	Full-width half-maximum (°)	Crystallite size (nm)	Microstrain ($\times 10^{-3}$)	Dislocation density ($\times 10^{-4}$ nm^{-2})
(A) Pure TiO_2	0.18	45.21	3.49	4.89
(B) 0.1 wt.% C-doped TiO_2	0.19	42.84	3.69	5.44
(C) 0.5 wt.% C-doped TiO_2	0.20	40.69	3.88	6.04

samples A, B, and C prepared by heat treatment was obtained using Raman spectrometry (Fig. 2). The four first-order Raman-active modes of vibration centered at 142.28 cm^{-1} (E_g), 394.4 cm^{-1} (B_{1g}), 515.67 cm^{-1} ($A_{1g}+B_{1g}$), and 636.94 cm^{-1} (E_g) correspond to the anatase phase of TiO_2.[38] The low-frequency phonon band of anatase TiO_2 centered at 142.28 cm^{-1} (E_g) was the dominant mode present in both pure and doped TiO_2 samples. The peak at 636.94 cm^{-1} (E_g) correspond to the symmetric stretching vibration of O–Ti–O in TiO_2. The peaks at 394.4 cm^{-1} (B_{1g}) and 515.67 cm^{-1} ($A_{1g}+B_{1g}$) are attributed to the symmetric and asymmetric bending vibrations of O–Ti–O in TiO_2.[39,40] The decrease in the intensity and broadening of the peaks at 144 cm^{-1}, 394.4 cm^{-1}, 515.67 cm^{-1}, and 636.94 $cm^{-1}$was observed for the carbon-doped samples. This may be due to the impurity and defects arising with increased carbon content in TiO_2.[41]

Field-Emission Scanning Electron Microscopy (FESEM) Analysis

The surface morphology of samples A, B, and C sintered at 600°C was examined using FESEM (Fig. 3a). The FESEM micrographs for samples A, B, and C showed a spherical shape, with agglomerated grains of varying sizes, forming a nanocluster. Using ImageJ software, the average particle size for samples A, B, and C was calculated as 43.23 nm, 40.25 nm, and 40.56 nm, respectively. The decrease in grain growth was due to the incorporation of carbon atoms in TiO_2 that restricted the expansion of crystallite size. Smaller particle sizes provide enhanced surface area. Samples B and C had more active surface sites for the reaction between the synthesized material's surface and the water molecule.[42] During the reduction of pure TiO_2, carbon may have diffused into the crystal lattice of TiO_2,

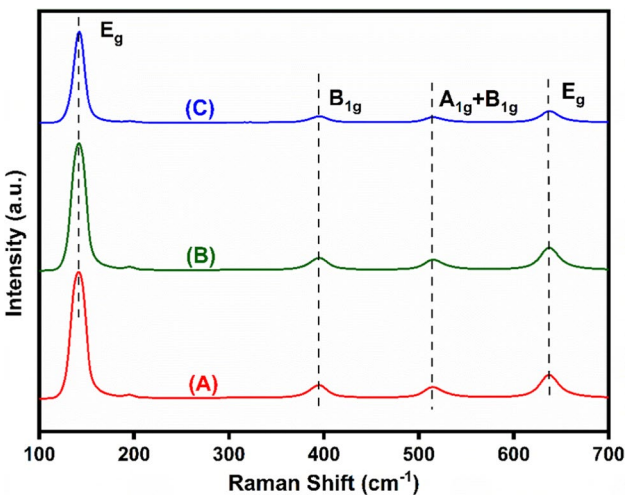

Fig. 2 Raman spectra of (A) pure TiO_2, (B) 0.1 wt.% carbon-doped TiO_2, and (C) 0.5 wt.% carbon-doped TiO_2.

resulting in a porous microstructure favorable for adsorption and chemidissociation[43] of water molecules on the surface of samples. Enhanced output power is produced when more water molecules are adsorbed and chemidissociated on the material's surface.

Photoluminescence (PL) Spectroscopy

An excitation wavelength of 320 nm was selected to study the defects arising in TiO_2 from carbon doping. High PL intensity typically suggests a higher carrier recombination rate. PL spectroscopy of the samples was performed at room temperature to investigate the presence of oxygen vacancies created by carbon doping. To eliminate emissions from the bandgap, the excitation energy used to obtain the PL spectra of samples A, B, and C was kept below their bandgap. Figure 4 shows the PL spectra of TiO_2 and carbon-doped TiO_2 nanoparticles. Ti^{4+} ions next to oxygen vacancies make up the majority of surface states.[44,45] A broad emission band in the region of 360–550 nm was observed for all the samples, which is attributed to the oxygen vacancies in the samples.[46] These oxygen vacancies acted as trapping sites which reduced the recombination rate of electron–hole pairs. Hence, with the doping of different amounts of carbon in TiO_2, the PL intensity of TiO_2 decreased.

Working Mechanism of the Hydroelectric Cell

Unsaturated cations (Ti^{4+}) and oxygen vacancies act as the dangling bonds on the material surface. These dangling bonds attract polar water molecules towards the surface.[47] The water (H_2O) molecules are chemidissociated to hydronium ions (H_3O^+) and hydroxide ions (OH^-) on the material surface. More water layers are physisorbed above the chemisorbed layer, facilitating proton hopping by the Grotthuss mechanism, whereby "excess" protons can diffuse through the hydrogen bonds of water molecules or other attached water by forming and simultaneously breaking covalent bonds with molecules in the vicinity.[48]

These hopping protons create strong electric fields when trapped inside the nano-pores present on the material's surface. This field is sufficient to dissociate water in the physisorbed layers. The physidissociated OH^- ions migrate towards zinc and oxidize it to zinc hydroxide with a release of two electrons. The standard oxidation potential of this reaction is 0.76 V. At the cathode, hydronium ions accept these electrons and are reduced to hydrogen gas with a standard reduction potential of 0.22 V. In HECs, reactions at the electrodes produce voltage and current. The chemical reactions occurring in the cell are as follows:

Dissociation of water molecules at the surface:

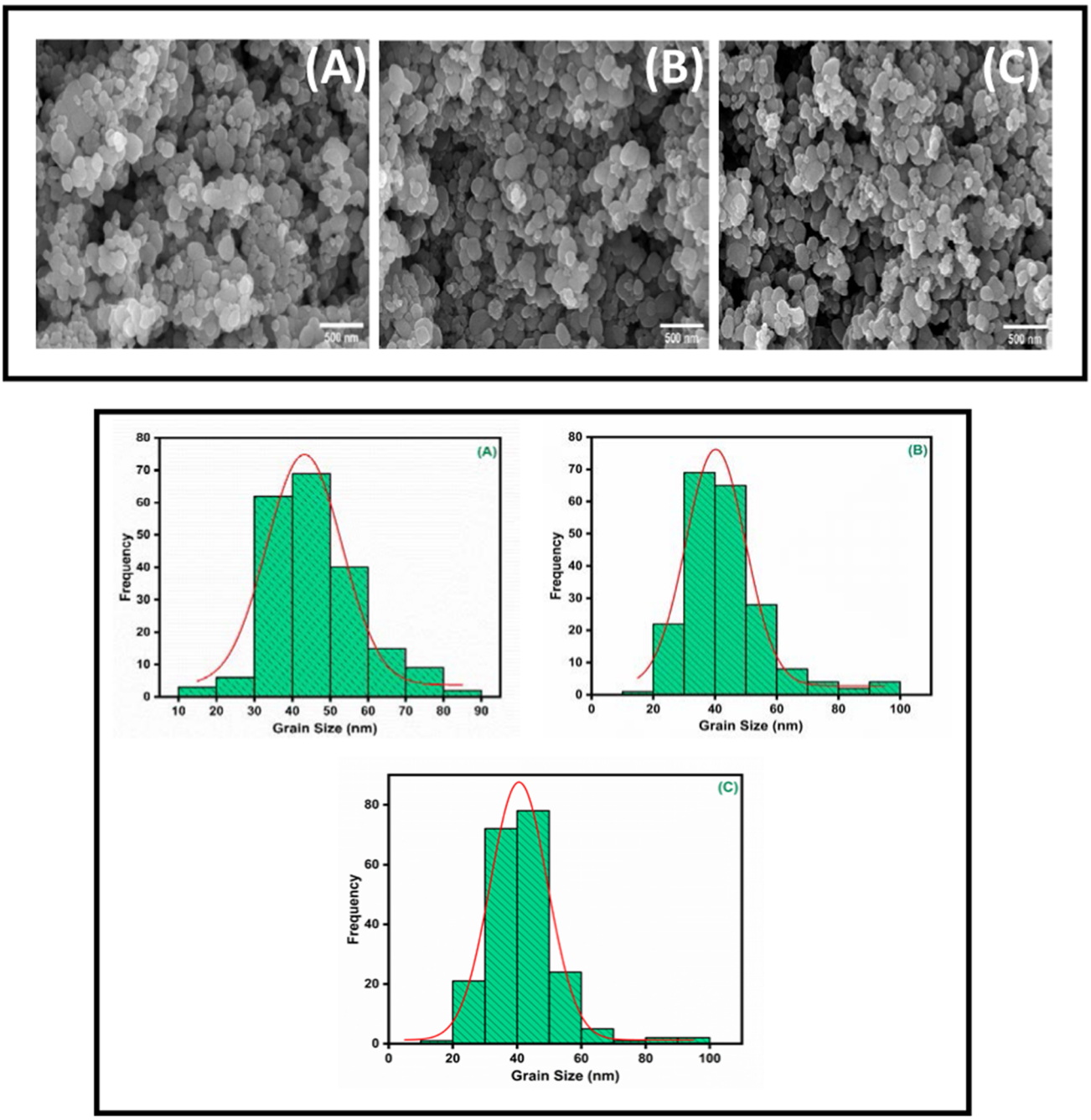

Fig. 3 (a) FESEM micrographs of (A) pure TiO_2, (B) 0.1 wt.% carbon-doped TiO_2, and (C) 0.5 wt.% carbon-doped TiO_2. (b) Histogram size distribution of (A) pure TiO_2, (B) 0.1 wt.% carbon-doped TiO_2, and (C) 0.5 wt.% carbon-doped TiO_2.

$$4H_2O \leftrightarrow 2OH^- + 2H_3O^+ \quad (4)$$

At the anode:

$$Zn + 2OH^- \rightarrow Zn(OH)_2 + 2e^- E_{oxd} = 0.76\,V \quad (5)$$

At the cathode:

$$2H_3O^+ + 2e^- \rightarrow H_2(g) + 2H_2O\,E_{red} = +0.22V \quad (6)$$

In samples B and C (carbon-doped TiO_2), more oxygen vacancies are created in their lattices than in the lattice of sample A (pure TiO_2), which is evident from the PL spectrum. The increased active surface enhanced the interaction

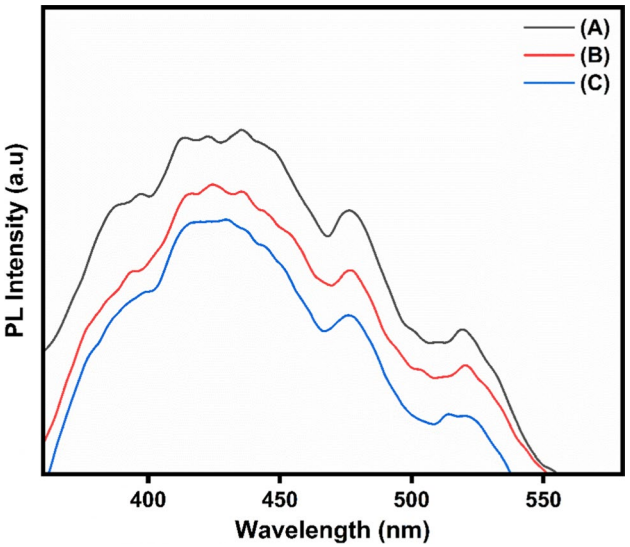

Fig. 4 Room-temperature PL emission spectra of (A) pure TiO_2, (B) 0.1 wt.% carbon-doped TiO_2, and (C) 0.5 wt.% carbon-doped TiO_2.

Table II Open-circuit voltage, short-circuit current, and off-load power of pure and carbon-doped TiO_2-based HECs

Hydroelectric cell	Open-circuit voltage (V)	Short-circuit current (mA)	Off-load power (mW)
(A) Pure TiO_2	0.76	5.0	3.8
(B) 0.1 wt.% C-doped TiO_2	0.81	6.3	5.1
(C) 0.5 wt.% C-doped TiO_2	0.74	7.0	5.2

sites between the water and material surface, which resulted in increased current in carbon-doped TiO_2-based HECs relative to the pure TiO_2-based HEC.

V–I Polarization Curve of the Hydroelectric Cell

The standard V–I polarization curves were plotted for pure TiO_2 and carbon-doped TiO_2-based HECs. The open-circuit voltage, short-circuit current, and off-load power for the cells are listed in Table II.

The V–I polarization exhibited different polarization regions[5] as shown in Fig. 5. The fabricated HEC of pure TiO_2 and 0.1 wt.% and 0.5 wt.% carbon-doped TiO_2 generated short-circuit current, open-circuit voltage, and off-load output power of 5.0 mA, 0.76 V, 3.8 mW; 6.3 mA, 0.81 V, 5.10 mW; and 7 mA, 0.74 V, 5.2 mW, respectively. The points K, P, and T denote the open-circuit voltage of the cells at infinite load. The decreasing voltage at regions KL, PQ, and TU represents the activation losses that occurred to overcome the energy barrier for the electrochemical reaction at the electrodes.[4] This can also be explained by the development of a double ionic layer at interfaces and the fact that charge transfer requires more power when there are fewer dissociated OH^- ions present.

The regions LM, QR, and UV represent the ohmic losses in the cells due to the internal resistance faced by the ions traveling through the porous material structure. The increased porosity in carbon-doped TiO_2, as evident in the SEM micrographs, increased the active surface area for spontaneous dissociation of water. Sample C exhibits high porosity, as shown in SEM micrographs, as well as oxygen vacancy defects evident from the PL spectra, which enable enhanced dissociation of water molecules. Hence, the HEC fabricated from sample C generated higher current of 7 mA relative to samples A and B, at 5 mA and 6.3 mA, respectively. The high-current-density regions MN, RS, and VW exhibited rapid voltage drops because of the accumulation of excess ions at the electrode interface,[4] which restrict mass transport. This rapid decrease in voltage is referred to as concentration loss or mass transport loss.

Electrochemical Impedance Spectroscopy (EIS)

The charge transfer mechanism and migration of dissociated ions taking place within the HECs were investigated by electrochemical impedance spectroscopy.[49] The Nyquist curves obtained for HECs fabricated with samples A, B, and C are shown in Fig. 6. At room temperature, complex impedance (Z'') was plotted against the real impedance (Z') for pure TiO_2 and carbon-doped TiO_2. The Nyquist plots were separated into two sections: (i) a high-frequency region comprising a semicircle which provides information about the charge resistance due to grains, grain boundaries, and other components and represents the total internal resistance of the cell for charge transfer; and (ii) a low-frequency region offering insights about the ionic diffusion process at the electrodes.[50] A small arc diameter indicates enhanced charge segregation and transfer, whereas the processes of ion diffusion and electron migration are increased with a straight loop or a tail.[51–53] Doping of carbon generates pores in TiO_2, resulting in the adsorption of more water molecules through oxygen vacancies on the surface of the sample.[54] Hence, carbon-doped TiO_2 (samples B and C)-based cells exhibit lower resistance than pure TiO_2. Wang et al.[55]noted that the Nyquist curve for sample B with a lower amount of carbon exhibited greater potential for charge transfer than sample C. This can be explained by the fact that when TiO_2 nanoparticles with a minimal amount of carbon were calcined for several hours, the carbon inside was distributed more uniformly and came into close contact with the inner surface. Sample C with higher carbon content therefore exhibited greater charge transfer resistance than sample B. The diffusion of ions at the electrode interface is indicated by the presence of tails in the Nyquist plots of both wet TiO_2 and carbon-doped TiO_2 cells at low frequency.[56,57]

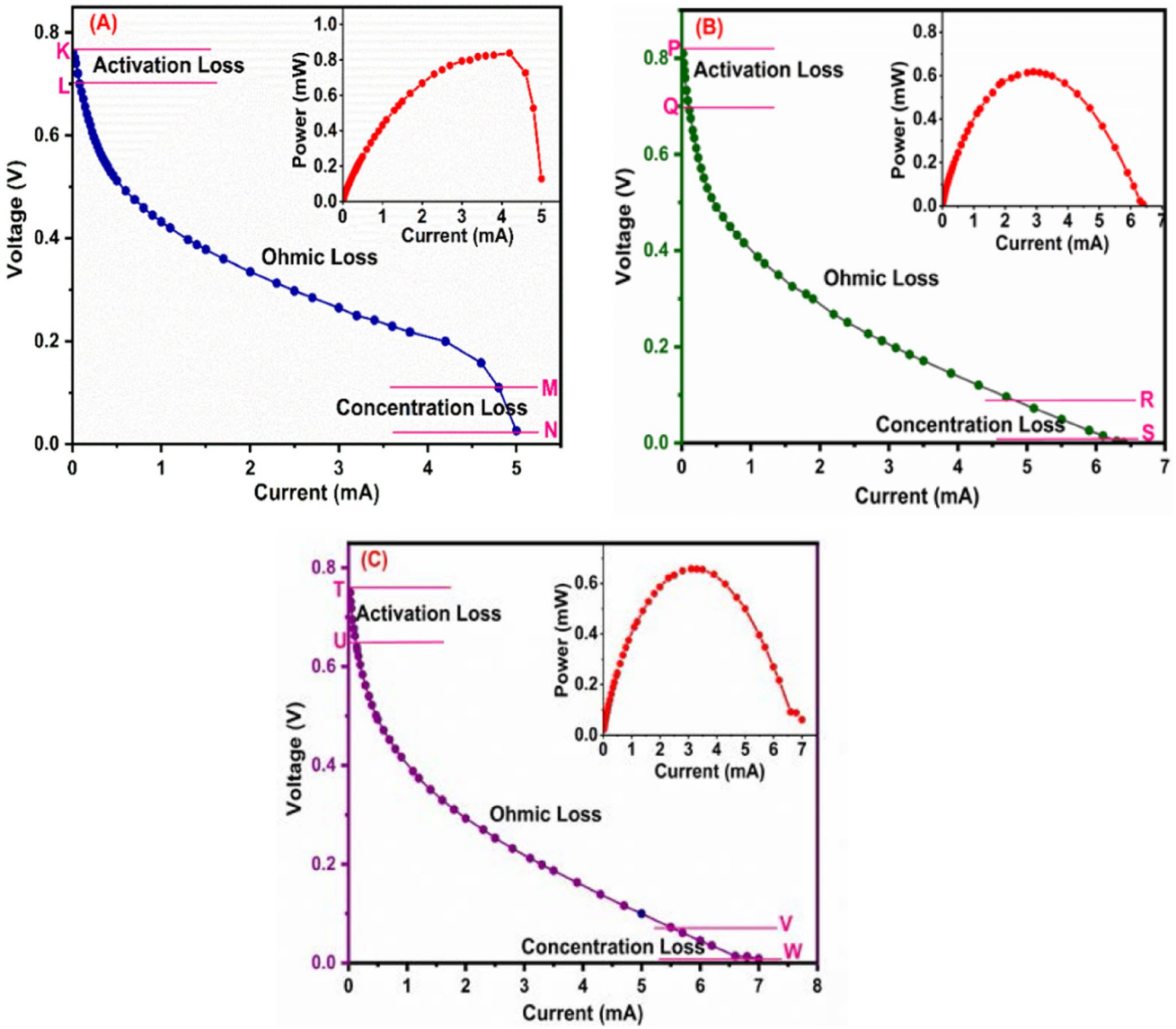

Fig. 5 V–I polarization curve generated by (A) pure TiO_2, (B) 0.1 wt.% carbon-doped TiO_2, and (C) 0.5 wt.% carbon-doped TiO_2-based hydroelectric cell soaked in distilled water.

Conclusions

Carbon-doped TiO_2 nanoparticles were synthesized by solid-state reaction. Carbon doping induced the formation of oxygen vacancies in TiO_2 and also enhanced the conduction within the material. The greater number of oxygen vacancies in the carbon-doped TiO_2 samples than pure TiO_2 is responsible for the splitting of a larger number of water molecules, resulting in increased green electricity generation by the fabricated hydroelectric cells. Higher material conductivity in carbon-doped TiO_2 facilitated the movement of dissociated ions towards the electrodes, which ultimately led to increased power output from the carbon-doped TiO_2 -based hydroelectric cells. Power output of 5.10 mW and 5.18 mW was obtained via water splitting by 0.1 wt.% and 0.5 wt.% carbon-doped TiO_2-based HECs, showing that this is a cost-effective, eco-friendly, and efficient method for the generation of green energy.

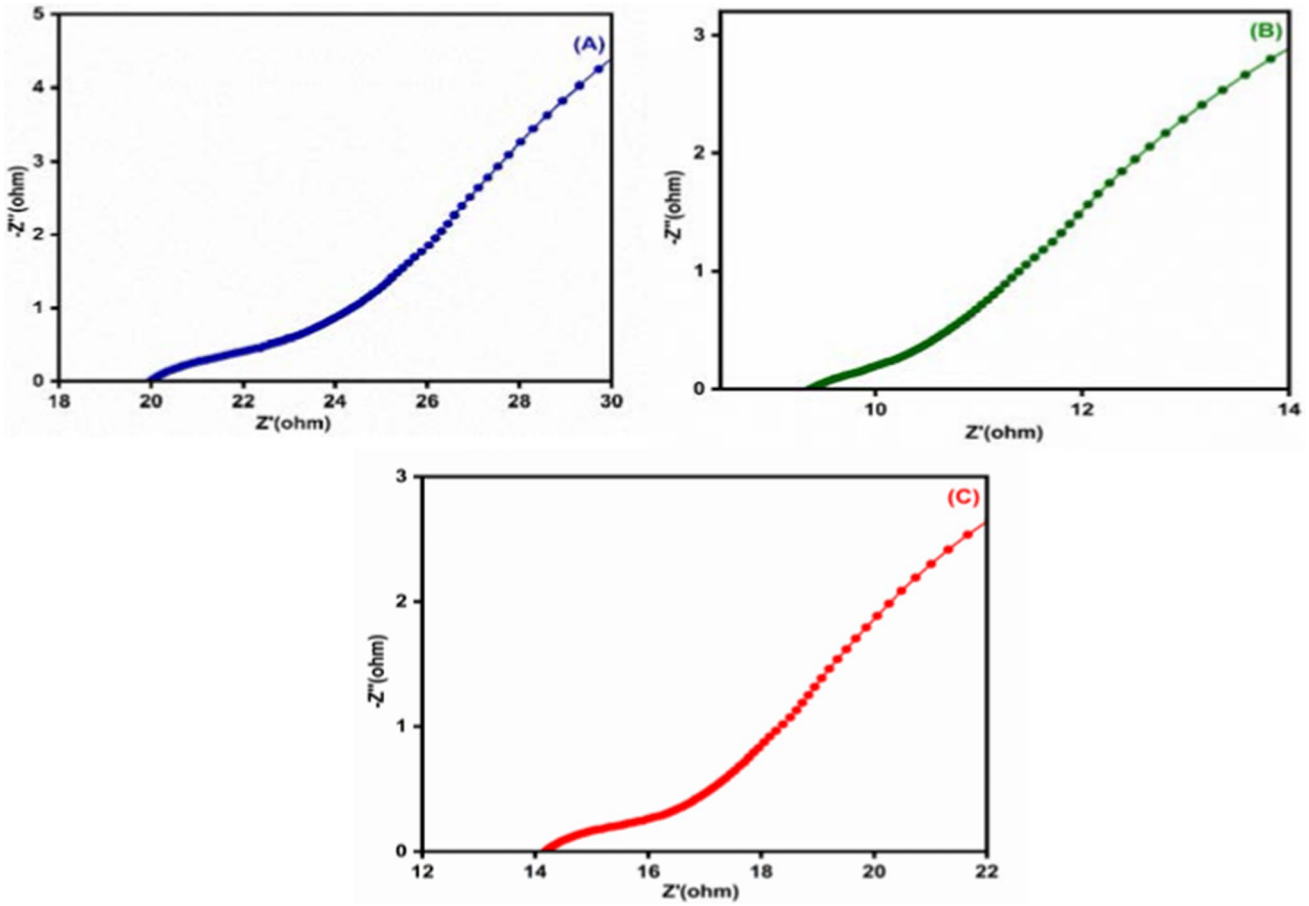

Fig. 6 Nyquist plots of (A) pure TiO_2, (B) 0.1 wt.% carbon-doped TiO_2, and (C) 0.5 wt.% carbon-doped TiO_2 -based hydroelectric cells.

Acknowledgments One of the authors, Prof. Rajesh Kumar, is highly thankful to Guru Gobind Singh Indraprastha University, New Delhi, India, for providing the FRGS to carry out this research work. Ms. Kajal is thankful to Guru Gobind Singh Indraprastha University, New Delhi, India, for providing the Short-Term Research Fellowship (STRF). The characterization facilities provided by Malaviya National Institute of Technology (MNIT), Jaipur, India, are gratefully acknowledged.

Conflict of interest No potential conflict of interest was reported by the authors.

Ethical approval Not applicable.

References

1. E. Kabir, P. Kumar, S. Kumar, A.A. Adelodund, and K. Kim, Solar energy: potential and future prospects. *Renew. Sustain. Energy Rev.* 82, 894–900 (2018).
2. K.M. Winslow, S.J. Laux, and T.G. Townsend, A review on the growing concern and potential management strategies of waste lithium-ionbattery. *Resour. Conserv. Recycl.* 129, 263–277 (2018).
3. C. Acar, I. Dincer, and G.F. Naterer, Review of photocatalytic water splitting methods for sustainable hydrogen production. *Int. J. Energy Res.* 40(11), 1449–1473 (2016).
4. R.K. Kotnala, and J. Shah, Green hydroelectrical energy source based on water dissociation by nanoporous ferrite. *Int. J. Energy Res.* 40, 1652–1661 (2016).
5. P. Kumar, S. Vashishth, I. Sharma, and V. Verma, Porous SnO_2 ceramic-based hydroelectric cells for green power generation. *J. Mater. Sci.: Mater. Electron.* 32, 1052–1060 (2021).
6. S. Saini, J. Shah, R.K. Kotnala, and K.L. Yadav, Nickel substituted oxygen deficient nanoporous lithium ferrite based green energy device hydroelectric cell. *J. Alloys Compd.* 827, 154334–154343 (2020).
7. J. Shah, K.C. Verma, A. Agarwal, and R.K. Kotnala, Novel application of multiferroic compound for green electricity generation fabricated as hydroelectric cell. *Mater. Chem. Phys.* 239, 122068 (2020).
8. R. Gupta, J. Shah, R. Das, S. Saini, and R.K. Kotnala, Defect-mediated ionic hopping and green electricity generation in Al_2–$xMgxO_3$-based hydroelectric cell. *J. Mater. Sci.* 56, 1600–1611 (2021).
9. U. Bhakar, A. Agarwal, S. Sanghi, J. Shah, and R.K. Kotnala, Production of green electricity from strained $BaTiO_3$ and TiO_2 ceramics based hydroelectric cells. *Mater. Chem. Phys.* 262, 124277 (2021).
10. S. Jain, J. Shah, N.S. Negi, C. Sharma, and R.K. Kotnala, Significance of interface barrier at electrode of hematite hydroelectric

cell for generating ecopower by water splitting. *Int. J. Energy Res.* 43(9), 4743–4755 (2019).
11. L.F. Bobadilla, J.L. Santos, S. Ivanova, J.A. Odriozola, and A. Urakawa, Unravelling the role of oxygen vacancies in the mechanism of the reverse water-gas shift reaction by operando DRIFTS and ultraviolet-visible spectroscopy. *ACS Catal.* 8(8), 7455–7467 (2018).
12. M. Gong, Y. Li, Y. Guo, X. Lv, and X. Dou, 2D TiO_2 nanosheets for ultrasensitive humidity sensing application benefited by abundant surface oxygen vacancy defects. *Sensors Actuators B Chem.* 262, 350–358 (2018).
13. W. Wu, J. Yao, S. Liu, L. Zhao, L. Xu, Y. Sun, Y. Lou, J. Zhao, J.H. Choi, and L. Jiang, Nanostructured hexagonal ReO_3 with oxygen vacancies for efficient electrocatalytic hydrogen generation. *Nanotechnology.* 30(35), 355701 (2019).
14. X. Pan, M.Q. Yang, X. Fu, N. Zhang, and Y.J. Xu, Defective TiO_2 with oxygen vacancies: synthesis properties and photocatalytic applications. *Nanoscale.* 5, 3601–3614 (2013).
15. Z. Wang, T. Zhang, T. Han, T. Fei, S. Liu, and G. Lu, Oxygen vacancy engineering for enhanced sensing performances: a case of SnO_2 nanoparticles-reduced graphene oxide hybrids for ultrasensitive Ppb-level room-temperature NO_2 sensing. *Sensors Actuators B Chem.* 266(2), 812–822 (2018).
16. N. Yamazoe, and Y. Shimizu, Humidity sensors: principles and applications. *Sensors and Actuators.* 10, 379–398 (1986).
17. J. Zhang, Z. Qin, D. Zeng, and C. Xie, Metal-oxide-semiconductor based gas sensors: screening, preparation, and integration. *Phys. Chem. Chem. Phys.* 19, 6313–6329 (2017).
18. R.P. Aloysius, V. Pandey, V. Verma, V.P.S. Awana, R.K. Kotnala, and P.C. Kothari, Structural and magnetic properties of A2-xBxFeMoO6: double perovskite CMR systems. *Sens. Lett.* 7, 224–231 (2009).
19. H. Ji, W. Zeng, and Y. Li, Gas sensing mechanisms of metal oxide semiconductors: a focus review. *Nanoscale* 11, 22664–22684 (2019).
20. Z. Chen, and C. Lu, Humidity sensors: a review of materials and mechanisms. *Sens. Lett.* 3, 274–295 (2005).
21. Y. Zhong, W. Li, X. Zhao, X. Jiang, S. Lin, Z. Zhen, W. Chen, D. Xie, and H. Zhu, High-response room-temperature NO_2 sensor and ultrafast humidity sensor based on SnO_2 with rich oxygen vacancy. *ACS Appl. Mater. Interfaces* 11(14), 13441–13449 (2019).
22 Y. Wang, N.H. Nguyen, and T. Truong, Mechanisms of and effect of coadsorption on water dissociation on an oxygen vacancy of the MgO (100) surface. *Chem. A Eur. J.* 12(22), 5859–5867 (2006).
23. H. Hu, H. Ji, and Y. Sun, The effect of oxygen vacancies on water wettability of a ZnO surface. *Phys. Chem. Chem. Phys.* 15(39), 16557 (2013).
24. R. Schaub, P. Thostrup, N. Lopez, E. Lægsgaard, I. Stensgaard, J.K. Nørskov, and F. Besenbacher, Oxygen vacancies as active sites for water dissociation on rutile TiO_2 (110). *Phys. Rev. Lett.* 87(26), 266104 (2001).
25. W. Yu, Z. Shen, F. Peng, Y. Lu, M. Ge, X. Fu, Y. Sun, X. Chen, and N. Dai, Improving gas sensing performance by oxygen vacancies in sub-stoichiometric WO3−x. *RSC Adv.* 9(14), 7723–7728 (2019).
26. M. Fronzi, S. Piccinin, B. Delley, E. Traversa, and C. Stampfl, Water adsorption on the stoichiometric and reduced CeO_2(111) surface: A first-principles investigation. *Phys. Chem. Chem. Phys.* 11(40), 9188 (2009).
27 W. Li, S. Liu, S. Wang, Q. Guo, and J. Guo, The roles of reduced Ti cations and oxygen vacancies in water adsorption and dissociation on $SrTiO_3$ (110). *J. Phys. Chem. C.* 118(5), 2469–2474 (2014).
28. R. Asahi, Y. Taga, W. Mannstadt, and A.J. Freeman, Electronic and optical properties of anatase TiO_2. *Phys. Rev. B.* 61, 7459–7465 (2000).
29. M. Koelsch, S. Cassaignon, C.T.T. Minh, J.F. Guillemoles, and J.P. Jolivet, Electrochemical comparative study of titania (anatase, brookite and rutile) nanoparticles synthesized in an aqueous medium. *Thin Solid Films* 451, 86–92 (2004).
30. O. Carp, C.L. Huisman, and A. Reller, Photoinduced reactivity of titanium dioxide. *Prog. Solid State Chem.* 32, 33–177 (2004).
31. A. Shukla, R. Das, R. Agrawal, G. Kotnala, S. Jain, R. Gupta, and J. Shah, Substitution in titanium dioxide hydroelectric cell induces higher green energy. *AKGEC Int. Jr. of Tech.* 10, 2 (2019).
32. A.L. Patterson, The scherrer formula for x-ray particle size determination. *Phys. Rev.* 56(10), 978–982 (1939).
33. M. Pal, U. Pal, J.M.G.Y. Jimenez, and F.P. Rodriguez, Effects of crystallization and dopant concentration on the emission behavior of TiO2: Eu nanophosphors. *Nanoscale Res. Lett.* 7(1), 1 (2012).
34. D.E.J. Cortazar, J.G. Torres-Torres, A.H. Ramirez, J.C.A. Pérez, A.C. Uribe, S. Godavarthi, A.E.E.D.L. Monteros, A.A.S. Pavón, and A.C. Garcia, Doping of TiO_2 using metal waste (Door key) to improve its photocatalytic efficiency in the mineralization of an emerging contaminant in an aqueous environment. *Water* 14(9), 1389 (2022).
35. S. Habibi, and M. Jamshidi, Sol–gel synthesis of carbon-doped TiO_2 nanoparticles based on microcrystalline cellulose for efficient photocatalytic degradation of methylene blue under visible light. *Environ. Technol.* 41, 3233–3247 (2019).
36. M. Hassan, S. Younas, F. Sher, S.S. Husain, S. Riaz, and S. Naseem, Room temperature ferromagnetism in single-phase Zn1− xMnxS diluted magnetic semiconductors fabricated by co-precipitation technique. *Appl. Phys. A Mater. Sci. Process.* 123, 352 (2017).
37. A.M. Alsaad, A.A. Ahmad, Q.M. Al-Bataineh, A.A. Bani-Salameh, H.S. Abdullah, I.A. Qattan, Z.M. Albataineh, and A.D. Telfah, Optical, structural, and crystal defects characterizations of dip synthesized (Fe-Ni) Co-doped ZnO thin films. *Materials.* 13(7), 1737 (2020).
38. T. Ohsaka, Temperature dependence of the Raman spectrum in anatase TiO_2. *J. Phys. Soc. Jpn.* 48, 1661–1668 (1980).
39. S. Weon, E. Choi, H. Kim, J.Y. Kim, H.J. Park, S.M. Kim, W. Kim, and W. Choi, Active 001 facet exposed TiO_2 nanotubes photocatalyst filter for volatile organic compounds removal: from material development to commercial indoor air cleaner application. *Environ. Sci. Technol.* 52(16), 9330–9340 (2018).
40. F. Tian, Y. Zhang, J. Zhang, and C. Pan, Raman spectroscopy: a new approach to measure the percentage of anatase TiO_2 exposed (001) facets. *J. Phys. Chem. C.* 116(13), 7515–7519 (2012).
41. G. Yang, Z. Jiang, H. Shi, T. Xiao, and Z. Yan, Preparation of highly visible-light active N-doped TiO_2 photocatalyst. *J. Mater. Chem.* 20, 5301–5309 (2010).
42. K.J. Antony Raj, and B. Vishwanathan, Effect of surface area, pore volume and particle size of P25 titania on the phase transformation of anatase to rutile. *Indian J. Chem.* 48A, 1378–1382 (2009).
43. J. Shah, S. Jain, B. Gahtori, C. Sharma, and R.K. Kotnala, Water splitting on the mesoporous surface and oxygen vacancies of iron oxide generates electricity by hydroelectric cell. *Mater. Chem. Phys.* 258, 123981 (2021).
44. G. Redmond, D. Fitzmaurice, and M. Graetzel, Effect of surface chelation on the energy of an intraband surface state of a nanocrystalline titania film. *J. Phys. Chem.* 97(27), 6951–6954 (1993).
45. A.L. Linsebigler, G. Lu, and J.T. Yates Jr., Photocatalysis on TiO_2 surfaces: principles, mechanisms, and selected results. *Chem. Rev.* 95(3), 735–758 (1995).

46. S.H. Alias, N.N. Mohamed, L.W. Loon, and S. Chandren, Synthesis of carbon self-doped titanium dioxide and its activity in the photocatalytic oxidation of styrene under visible light irradiation. *Malays. J. Fundam. Appl. Sci.* 15(2), 291–297 (2019).
47. K.G. Godinho, A. Walsh, and G.W. Watson, Energetic and electronic structure analysis of intrinsic defects in SnO_2. *J. Phys. Chem. C* 113, 439–448 (2009).
48. E.C. Hernández, and P.G. Kusalik, Probing the mechanisms of proton transfer in liquid water. *Proc. Natl. Acad. Sci. USA* 34(110), 13697–13698 (2013).
49. R.K. Kotnala, R. Gupta, A. Shukla, S. Jain, A. Gaur, and J. Shah, Metal oxide-based hydroelectric cell for electricity generation by water molecule dissociation without electrolyte/acid. *J. Phys. Chem. C.* 122, 18841–18849 (2018).
50. Y. Ma, M. Ni, and S. Li, Optimization of malachite green removal from water by TiO_2 nanoparticles under UV irradiation. *Nanomaterials* 8, 428 (2018).
51. C.A. D'Amato, R. Giovannetti, M. Zannotti, E. Rommozzi, S. Ferraro, C. Seghetti, M. Minicucci, R. Gunnella, and A.D. Cicco, Enhancement of visible-light photoactivity by polypropylene coated plasmonic Au/TiO_2 for dye degradation in water solution. *Appl. Surf. Sci.* 441, 575–587 (2018).
52. G. Darabdhara, P.K. Boruah, P. Borthakur, N. Hussain, M.R. Das, T. Ahamad, S.M. Alshehri, V. Malgras, K.C.W. Wu, and Y. Yamauchi, Reduced graphene oxide nanosheets decorated with Au–Pd bimetallic alloy nanoparticles towards efficient photocatalytic degradation of phenolic compounds in water. *Nanoscale* 8, 8276–8287 (2016).
53. C. Li, X. Zhu, H. Zhang, Z. Zhu, B. Liu, and C. Cheng, 3D ZnO/Au/CdS sandwich structured inverse opal as photoelectrochemical anode with improved performance. *Adv. Mater. Interfaces* 2, 1500428 (2015).
54. A. Gaur, A. Kumar, P. Kumar, R. Agrawal, J. Shah, and R.K. Kotnala, Fabrication of a SnO_2-based hydroelectric cell for green energy production. *ACS Omega* 5(18), 10240–10246 (2020).
55. W. Wang, D. Xu, B. Cheng, J. Yu, and C. Jiang, Hybrid carbon@TiO_2 hollow spheres with enhanced photocatalytic CO_2 reduction activity. *J. Mater. Chem. A.* 5, 5020–5029 (2017).
56. J.H. Jang, S. Yoon, H.K. Bok, Y.H. Jung, and S.M. Oh, Complex capacitance analysis on leakage current appearing in electric double-layer capacitor carbon electrode. *J. Electrochem. Soc.* 152, A1418–A1422 (2005).
57. P. Los, A. Lasia, H. Menard, and L. Brossard, Impedance studiesof porous lanthanum-phosphate-bonded nickel electrodes in concentrated sodium hydroxide solution. *J. Electroanal. Chem.* 360, 101–118 (1993).